# The role of interfacial properties on MEMS performance and reliability

M. P. de Boer, J. A. Knapp, T. M. Mayer and T. A. Michalske
Sandia National Laboratories, Albuquerque, NM 87185

www.mdl.sandia.gov/Micromachine

**ABSTRACT**

We have constructed a humidity-controlled chamber in which deflections of polysilicon cantilever beams are observed by interferometry, resulting in *in-situ* adhesion measurements within a fracture mechanics framework. From adhesion energy measurements for uncoated hydrophilic beams, we demonstrate an exponential dependence of adhesion on relative humidity (RH). We can explain this trend with a single-asperity model for capillary condensation. For coated hydrophobic beams, adhesion is independent of RH up to a threshold value which depends on the coating used. However, we have found that exposure to very high RH (=90%) ambients can cause a dramatic increase in adhesion, surprisingly with a stronger effect for perfluorodecyltrichlorosilane (FDTS, $C_{10}H_4F_{17}SiCl_3$) than octadecyltrichlorosilane (ODTS, $C_{18}H_{37}SiCl_3$). Newly developed computational mechanics to measure adhesion in the presence of an applied load allow us to explore how the adhesion increase develops. We believe that water adsorption at silanol sites at the FDTS/substrate interface, possibly exacerbated by coupling agent migration, leads to water islanding and the subsequent adhesion increase at very high RH levels.

## 1. INTRODUCTION – FOR RELIABLE MEMS, ADHESION MUST BE WELL UNDERSTOOD

In Microelectromechanical Systems (MEMS), surface forces can play a relatively large role compared to gravity and inertia, which are the dominating forces at the macroscale. This is due to the large increase in surface to volume ratio at the microscale. Because surface forces are not well characterized and often difficult to reproduce in MEMS structures, most commercial applications avoid contact between structural members. Examples include accelerometers and gyroscopes [1-3]. An important commercial device in which adhesive contact between moving structures and the substrate is allowed is the Digital Mirror Device [4]. For this product, adhesion (e.g., stiction) and adhesion hysteresis (changes in adhesion over time or due to environment) are important factors in determining device reliability.

At Sandia National Laboratories, we have interest in a multitude of devices which may allow contact between structural members. These systems can be actuated by electrostatic comb [5], wedge stepper [6] and rotary [7] micromotors. Our applications are in the fields of optics [8-10], device safing [11], and inertial sensing [12]. Both the actuators themselves as well as the devices they drive can potentially have contact between structures which are intended to transfer force. Therefore a key interface in MEMS is that which is created when two surfaces, constructed separately, come together.

There are many performance and reliability issues associated with such devices. Besides operational contact, surfaces in these devices may also come into contact while in storage due to shock, electrostatics or capillary action. Adhesive forces can then develop which prevent their subsequent function. The first concern is therefore with adhesion at the interface created when two surfaces come into contact. Our work is guided by the following questions. (1) Will these devices function properly after they have been in storage for a given period of time? (2) What is the effect of environment on the devices? Because the exact eventual implementation of devices is as yet unclear, we have chosen to concentrate on fundamental aspects to these questions through the use of simple cantilever beam test devices. Our framework for the measurement of adhesion stems from the discipline of fracture mechanics.

In this paper, we will describe an Environmental Interferometric Microprober which we constructed to make adhesion measurements, and demonstrate an accurate method for measuring adhesion of MEMS structure with this apparatus. We will then explore the dependence of adhesion on ambient, concentrating our effort on the effects of humidity. First we shall study untreated hydrophilic surfaces, and find that adhesion is exponential with RH. Next, we shall study coated surfaces, and determine their operational range with respect to RH, as well as the mechanisms which limit this range. Finally, we shall explore a more advanced method to measure adhesion along the length of the beam, which allows us to quantify adhesion hysteresis.

## 2. INTERFEROMETRY IS AN IDEAL TOOL FOR MEASURING ADHESION IN MEMS

We require a metrology with which we can measure deflections appropriately at the microscale. The cantilever beams we employ for adhesion measurement are hundreds of microns long, and simple optical microscopy is a suitable tool to measure in-plane dimensions. However, the beams are suspended only a few microns above the substrate, and knowledge of their out-of-plane deflections is essential to obtaining accurate adhesion values as we shall see in the following section. By adding a Michelson attachment to the optical objective, we obtain interferograms which give us out-of-plane information on deflections because fringe information is superposed on the optical image. From a peak to a valley in the fringe intensity, the out-of-plane deflection is $\lambda/4$=137 nm for $\lambda$=547 nm. With digitized images, we obtain 10 to 50 points of varying intensity between each peak and valley, and interpolate these for enhanced resolution. Theoretical resolution is in the 10 nm range for this scheme. We shall see that a great deal about interfacial forces can be learned at this level of precision.

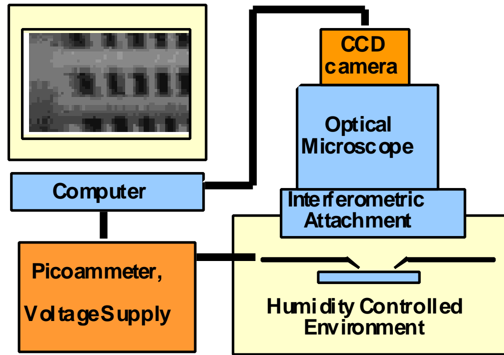


Fig. 1 Schematic of Environmental Microprober

To study adhesion in various ambients, we constructed an Environmental Interferometric Microprober as shown in Fig. 1. Probes were designed and constructed to fit under the 5 mm free working distance between the interferometric attachment and the sample. Magnification including the eyepiece is 50X (or 200X), and resolution is approximately 3 µm (or 1 µm) in the plane of the sample. Tilt of the interferometer reference surface is adjusted such that background fringes on the substrate are parallel to the length direction of the cantilever beams. Then, fringes on the cantilever beams are perpendicular to the beam length and directly indicate out-of-plane displacements. We seal the chamber from the ambient with a membrane between the Michelson attachment and the chamber. Humidity is introduced by flowing $N_2$ gas through a stainless steel water vessel heated to 50 °C, and the relative humidity (RH) level is controlled by combining it with dry $N_2$. RH data is obtained automatically by a computer monitored probe. At a given RH and exposure time, interferograms are recorded on a computer controlled CCD camera. Fringe patterns are subsequently quantified on individual cantilever beams, and analyzed using a computer program. Besides being very useful for adhesion measurements, this apparatus is valuable for extraction of mechanical properties as well as support post compliance to high confidence [13].

## 3. S-SHAPED CANTILEVERS ARE PREFERRED FOR ADHESION MEASUREMENT

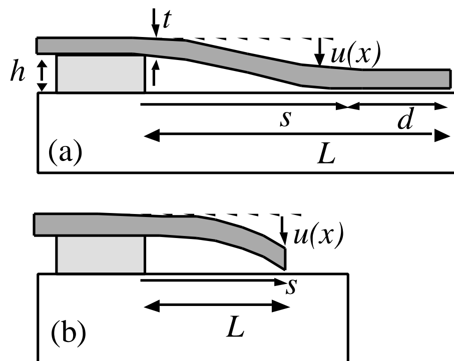


Fig. 2 (a) S-shaped and (b) arc-shaped beams

**3.1 Adhered cantilevers are S or arc-shaped.** In our initial work [14], we studied the two cantilever beam configurations proposed by Mastrangelo and Hsu [15], and represented in Fig. 2. We call these the S-shape (Fig. 2(a)) and arc-shape (Fig. 2(b)) cantilever beams. From our fracture mechanics perspective, we call the unadhered length $s$ in Fig. 2 the crack length. An energy analysis [14] indicates that only S-shaped or arc-shaped beams are possible – the transition between the two configurations is abrupt, and below a certain transition length, all adhered beams are in the arc shape. For typical values of micromachined surfaces, the attachment length $d\tilde{}\ L\text{-}s$ of the longest arc-shaped beam is only ˜ 0.1 µm, and decreases to zero for the shortest adhered beam.

**3.2 Fracture mechanics perspective.** Previous research [15-21] has concentrated on use of the arc-shape beam to measure adhesion, by measuring the shortest beam which is adhered. Fracture mechanics measurements depend on crack increments ?*s* being well defined. The calculated value of *d* is much shorter than the average distance between asperity peaks of typical micromachined surfaces for arc-shaped beams. Use of the shortest arc-shaped beam for adhesion measurements is suspect because the true contact area depends on the details of the particular topography in the adhered region of each arc-shaped beam. On the other hand, for S-shaped beams, the attachment length *d* is typically many tens of microns long. Crack extensions on the order of microns can be measured well, and at this scale the local interface probed by the crack tip at *s* will on average be the same from one beam to another. Therefore, particulars of the surface topography should have only a weak effect on the adhesion measured. Furthermore, a fracture equilibrium will be attained whether the crack length is initially greater or less than its

equilibrium value. Short arc-shaped beams may pop off the substrate, and a fracture equilibrium is inaccessible if this occurs. A further complication is the adhesion measured from a drying liquid, where capillary effects play a role in addition to the roughness. We shall address this issue later in this section.

**3.3 Adhesion measurement with interferometry.** We assess the adhesion of the two beam configurations as follows. First, we confirm that the beam deflections are those predicted from elasticity theory which assumes a JKR [22] adhesive interface (i.e., adhesive forces exist only between contacting surfaces). The deflections $u(x)$ are

$$u(x) = h\left(\frac{x}{s}\right)^2\left(3-2\frac{x}{s}\right) \text{ for S-shaped beams (1a), and } u(x) = \frac{h}{2}\left(\frac{x}{s}\right)^2\left(3-\frac{x}{s}\right) \text{ for arc-shaped beams (1b).}$$

where $h$, $t$, and $s$ are defined in Fig. 2. Second, we apply the equations

$$\Gamma = \frac{3}{2}E\frac{t^3h^2}{(s*)^4} \text{ for S-shaped beams (2a), and } \Gamma = \frac{3}{8}E\frac{t^3h^2}{(s*)^4} \text{ for the shortest arc-shaped beam (2b)}$$

where $\Gamma$ is the adhesion in μJ/m$^2$, $s*$ is the equilibrium crack length and $E$=170 GPa [23] is Young's Modulus.

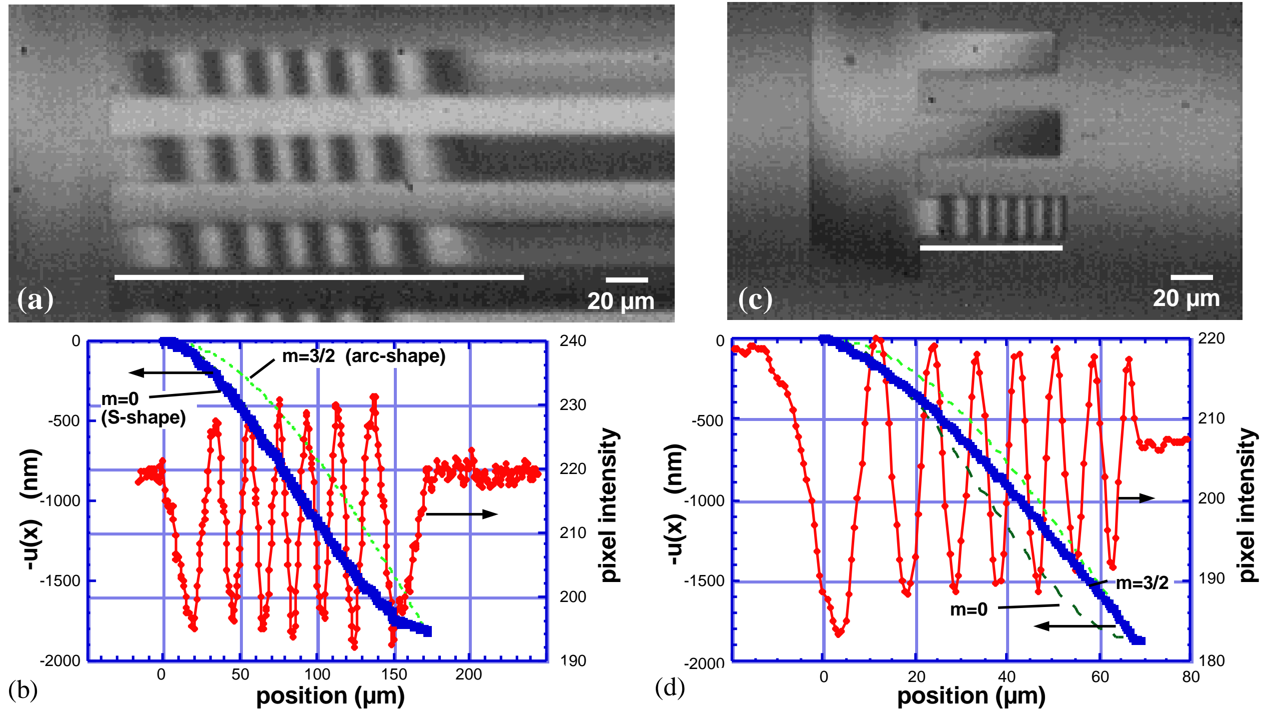

Fig. 3(a)-(d) beam deflections for S-shaped and arc-shaped beams

Results for polysilicon beams released in hydrofluoric acid, oxidized in hydrogen peroxide and transferred to water and dried in air are shown in Fig. 3. Here, the capillary action of the drying water acts to pull the beams into contact with the substrate. Fig. 3(a) is an optical interferometric image showing S-shaped adhered beams. Intensity versus position data from a linescan taken along the beam designated by a white line in Fig. 3(a) are plotted in the graph of Fig. 3(b) (right hand y-axis). The beam comes into contact with the substrate at the point where the linescan flattens out, at $x$=172.4 μm, ($u$=1820 nm). From the linescan data, $u$ deformations are computed and are plotted as a solid line referenced to the left-hand axis of Fig. 3(b). For comparison, predicted deformations for the extremes of the S and arc-shaped beams using Eq. (1) are also plotted using dashed lines. We see that the actual deformations agree well with those predicted for the S-shaped beams. Knowing that the deflections agree reasonably well with Eq. (1a), Eq. (2a) applies. Using measured values of $s*$=172.4 μm, $h$=1820 nm, $t$=2.3 μm, a first order adhesion value of $\Gamma$=11.3 mJ/m$^2$ is calculated.

The shortest value of $L$ for which beams remained adhered was 58 µm. If Eq. (2b) is used to quantify $\Gamma$ for this case, the first order result is that $\Gamma = 222$ mJ/m$^2$. However, as seen in Fig. 3(d) (for the case of a 68 µm long beam), the measured deformations lie somewhere between that predicted by the arc and S-shape limiting conditions. This change in deformation behavior is due to the compliance of the step-up post, which is expected to be non-negligible for beams below 100 µm in this geometry [24]. Compliance in the step-up post reduces the strain energy that is stored in the beam and hence the calculation for adhesion according to Eq. (2b) requires a correction. Although a much smaller effect, the step-up post compliance is also non-zero for case of S-shaped beams, Fig. 3(b). By using the measured slope at the beginning of the beam and matching the actual beam deformations to account for the step up post compliance in both the S-shape and arc-shape cases, we correct the values of adhesion. The correction decreases $\Gamma$ from 11.3 to 9.4 mJ/m$^2$ for the S-shaped beams, and from 222 to 91 mJ/m$^2$ for the arc-shape beams.

**3.4 Adhesion depends on the beam configuration.** Note that adhesion $\Gamma$ remains a factor of ten different even after this correction! Therefore, the values measured by the two beam configurations *are not equivalent!* We believe the observed difference between apparent adhesion values is related to the drying process itself. As water evaporates from the contact region of arc-shaped beams, impurities will necessarily concentrate in the capillary drop at the tip of the beam. In the limit as the capillary volume vanishes, impurities or solubility products may actually precipitate and lead to the possible formation of a porous solid network in the vicinity of the tip of the beam. Previous fracture mechanics measurements [25] have shown that precipitation of soluble silicates can support stress across solid silicate interfaces. In this scenario, the effective contact area can become much larger than the calculated value leading to an overestimate of the surface energy. Again, the extremely small contact region in the arc-shaped beam makes this measurement approach very sensitive to the nature and size of the contact region. S-shaped beams with their extended adhesive interface are expected to be much less sensitive to such effects.

**3.5 Advantages of the S-shape.** Besides a true fracture equilibrium and direct confirmation of beam deflections, there are several other advantages to interferometry using the S-shaped beam for adhesion measurement. First, the area consumed for adhesion measurement is much smaller – only a single beam is required. This is advantageous because of the expense of real estate on a MEMS chip. Second, the standard deviation for adhesion measurement is acquired in a straightforward fashion, because each beam gives a value for $\Gamma$. This provides adhesion uniformity information on a local scale. Third, as we shall see next, there is a great latitude in making adhesion measurements for this configuration with regard to environmental conditions.

## 4. WHY IS $\Gamma$ LESS THAN $2\gamma_{water}$ FOR A HYDROPHILIC SURFACE?

**4.1 Adhesion of $2\gamma_{water}$ is expected.** The surface in the above example is fully hydrophilic, and drying occurs last at the crack tip where capillary condensation. Laplace pressure lowering should give rise to a very slow evaporation of water in that locale. One might expect that the value for $\Gamma$ should be twice the surface energy of water, i.e., $\Gamma = 2\gamma_{water} = 146$ mJ/m$^2$. However, a value of $\Gamma = 9.4$ mJ/m$^2$ is measured. Why is the value from the S-shape configuration so much lower than $2\gamma_{water}$?

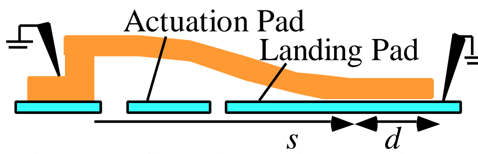

Fig. 4 Cantilever beam with actuation pad

**4.2 Adhesion vs. RH experiment.** To answer this question, we conducted experiments on beams which were initially freed by a supercritical $CO_2$ drying ($SCCO_2$) procedure [26]. Samples were rendered uniformly hydrophilic after $SCCO_2$ treatment by an oxygen plasma clean [27]. The cantilever beams were brought into contact with an actuation pad near the support post as shown in Fig. 4. After the actuation voltage was removed, the beams remain adhered due to adhesive forces only because the landing pad and cantilever are electrically grounded together.

The beams were first placed in a 0% RH ambient for 16 hours to minimize water adsorbed from the ambient. Next, the beams were pulled into contact with the landing pad. Because the beams are at least 1000 µm long, the beams remain in contact over a long length (i.e. they are S-shaped) with crack lengths are on the order of 600-850 µm, corresponding to $\Gamma = 68$-$17$ µJ/m$^2$ respectively. The RH was increased to 30%, and crack length began to decrease due to capillary action at the crack tip. After 40 hours, no further decrease was observed with $s^* \sim 300$ µm as seen in Fig. 5(a). RH was subsequently increased to 45, 55, 70 and 95%, and at each RH an equilibrium crack length $s^*$ was attained within 24-40 hours before increase to the next RH as seen in Figs. 5(b) and (c).

**4.3 Adhesion is exponentially dependent upon RH.** The beam validation and measurement procedure described above was repeated for each of five beams at the five different RH values ranging from 30 to 95%, and is plotted in Fig. 6 (as indicated by "Data"), where each line represents an individual beam at different RH values.

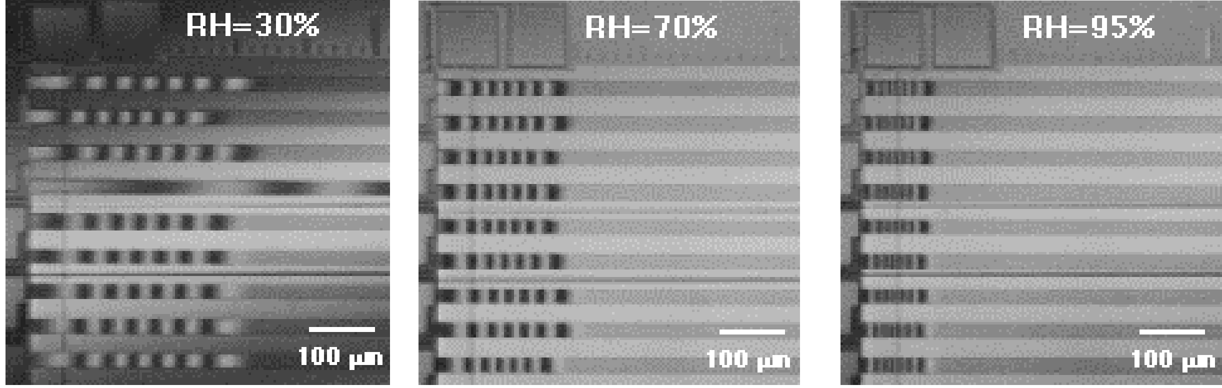

Fig. 5 Interferograms of crack length vs. RH after 40 hours exposure

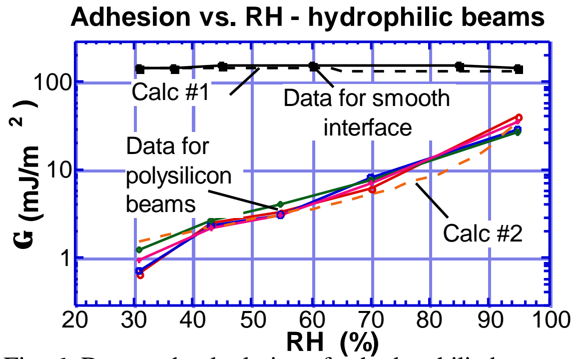

Fig. 6 Data and calculations for hydrophilic beams

In Fig. 6, we see that the dependence of adhesion on RH is exponential.

**4.4 For a smooth surface, adhesion is independent of RH.** The Kelvin equation predicts the radius of a capillary in a narrow channel as a function of RH. We investigated two possibilities for how the Kelvin equation might explain our results. In the first model, we assume that the interface between the beams is smooth, such that a microcapillary extends across the width of the beam at the crack tip and exerts a tensile pressure $q$ according to the Laplace equation. This is schematically represented in Fig. 7. For standard conditions, the radius of the capillary and the tensile force $q$ it exerts are [27]

$$r_K = \frac{1.04}{\ln(\mathrm{RH})}\,\mathrm{nm}, \qquad (3) \qquad \text{and} \qquad q = \frac{2\gamma_{water}\cos\theta}{r_K} = \frac{0.146}{r_K}\frac{\mathrm{N}}{\mathrm{m}^2} \qquad (4).$$

Here $r_K$ is the Kelvin radius in nm, RH varies from 0 to 1 for 0 to 100%, and the contact angle of water with the surface is $\theta=0°$. Eqs. (3) and (4) show that as RH increases, $r_K$ increases (the capillary spreads over a greater length under the beam), but the Laplace pressure $q$ decreases. Due to the offsetting effects, *adhesion is independent of RH under the assumptions of this smooth beam theory* [27], and this result is represented as "Calc #1 in Fig. 6. This is in good agreement with experiments on the crack healing and repropagation of glass [28] as shown in Fig. 6, and is a reasonable comparison to make because the oxidized polysilicon surface is glass. The reason for this good agreement is that glass fractures in an atomically smooth fashion.

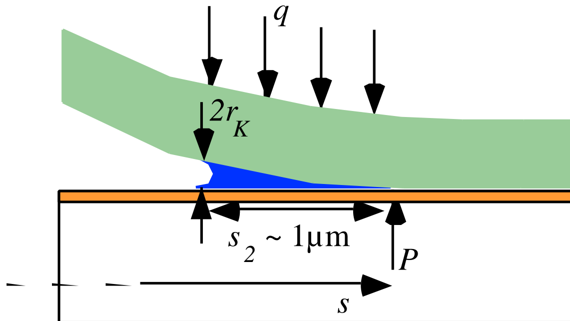

Fig. 7 Capillary in smooth interface – Calc #1

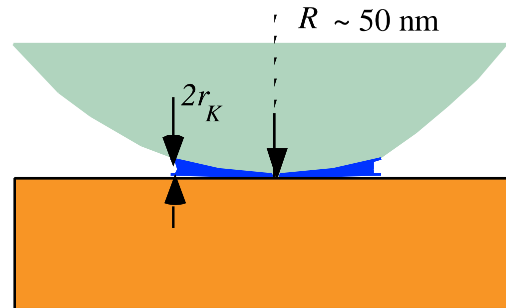

Fig. 8 Capillary in rough interface – Calc #2

**4.5 Roughness must be considered to explain the trend.** Nonetheless, the data from the experiment on the beams is clearly different from Calc #1. To explain the experimental trend, we must recognize that the polysilicon surface is inherently rough. While the rms roughness is 2-3 nm for our polysilicon, the radius of curvature $R$ of individual asperities is on the order of 50 nm. This is much larger than the Kelvin radius $r_K$ which is 1-20 nm over the

experimental 30-95% RH range, as represented in Fig. 7. Under these conditions, the interfacial energy per wetted asperity contact can be shown to be [29]

$$W_{Asp} = 8\pi\gamma_{water} R\, r_K \quad (5), \qquad \text{and adhesion is} \quad \Gamma \approx W_{Asp} n_{Asp} = -n_{Asp} \frac{0.94\,\mathrm{X}10^{-16}}{\ln(\mathrm{RH})} \frac{\mathrm{J}}{\mathrm{m}^2} \quad (6).$$

where $n_{Asp}$ is the number of contacting asperities per unit area. Eq. (6) is also plotted in Fig. 6 assuming $n_{Asp}$=20 per μm$^2$ and is labeled as "Calc #2". This shows a much improved trend in comparison with the experimental data.

The agreement of Calc #2 with the experimental data shows that roughness plays a strong role in determining the adhesion of hydrophilic polysilicon beams under humidified conditions. Further, the interferograms of Fig. 5 show the latitude of the experimental technique – each S-shaped beam gives an adhesion value at each RH value.

Why is $\Gamma < 2\gamma_{water}$ for beams dried from water in air? The results suggest that the local humidity condition at the crack tip during drying attains a level below that of saturation. The single asperity model explains the experimental trend well. However, further work is required to understand the data in detail. First, compared to atomic force microscope linescans, the value of $n_{Asp}$=20 per μm$^2$ appears to be somewhat high – one would expect a value closer of $n_{Asp}$~ 1 per μm$^2$. Second, as RH increases, multiple layers of water begin to adsorb on the surface. This should increase $n_{Asp}$ as RH increases. We will continue work to understand the data in quantitative fashion.

## 5. ADHESION PERFORMANCE OF SILANE COUPLING AGENTS AT HIGH RH

**5.1 Hydrophobic coatings reduce the susceptibility to water**: The values of adhesion observed for hydrophilic polysilicon beams in section 4 are in the mJ/m$^2$ range. Such high values can result in failure of many compliant micromechanisms. A remedy to this problem is to coat beams with silane coupling agents such as ODTS ($C_{18}H_{37}SiCl_3$) or FDTS ($C_8F_{17}C_2H_4SiCl_3$), in which the silicon headgroup hydrolyzes and attaches to a thin oxide formed on the silicon surface, leaving *hydrophobic* hydrocarbon or fluorocarbon tail groups of low surface energy exposed. ODTS is of interest as an adhesion promoter in glass reinforced composites [30], as an agent in improving selectivity in chromatographic separations [31], as a means to lower friction coefficients of tribological coatings [32,33], and has more recently been applied to MEMS in order to reduce adhesion and friction [34,35]. However, FDTS may have greater promise for integration in MEMS, particularly because of its ability to withstand air temperatures up to 400 °C, common in the packaging process [21]. A hitherto unaddressed question is the susceptibility of the coatings to adhesion degradation at high humidity levels.

A schematic of the solution deposition of the molecular coating is shown in Fig. 8. In principle, the molecules assemble into an ordered film on the surface due to head group interactions with the surface and cross polymerization, as well as van der Waal's attraction between the tail group. For these hydrophobic coatings, the surface energy $\gamma_s$ is reduced relative to the hydrophilic case, and the interfacial energy $\gamma_{ls}$ between water and the coating is much larger. The situation is represented in Fig. 9. Because of the high interfacial energy, the contact angle between water and the surface is greater than 90°. The contact angle is a macroscopic measure of average interfacial energy between the surface and the liquid. In the macroscopic sense, it is thermodynamically unfavorable to nucleate water on the surface in this hydrophobic case. Therefore, RH should have no effect on adhesion.

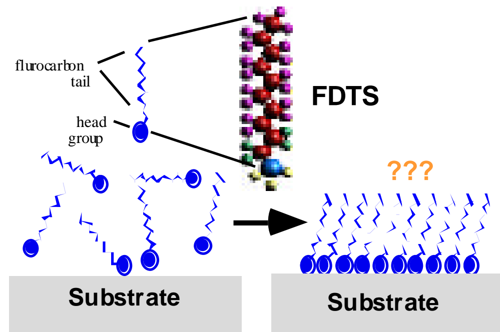


Fig. 8 Schematic of FDTS deposition

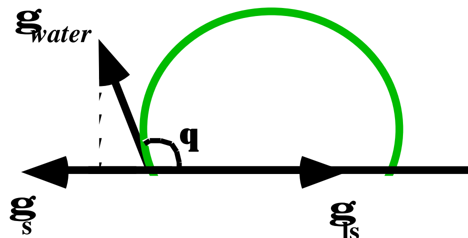


Fig. 9 Water nucleation on a hydrophobic surface is not favored

We suspect that microscopic aspects of the surface and film structure may influence the expectations from the simple macroscopic description just given. Although a large body of literature on this subject reflects the intensive study on these films [31,36-42], our understanding of the formation and structure of siloxane films is rather

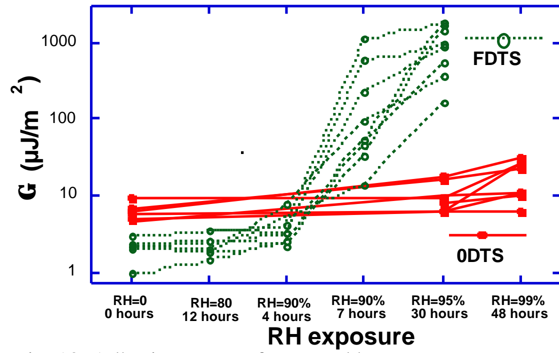

Fig. 10 Adhesion vs. RH for coated beams

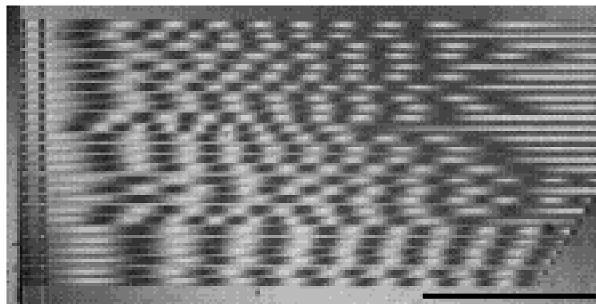
(a) 80% RH , 10 hour exposure 500 µm

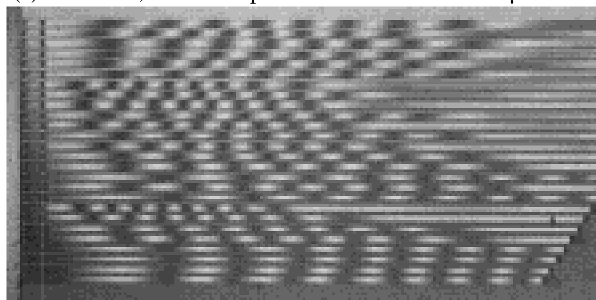
(b) 90% RH , 4 hour exposure

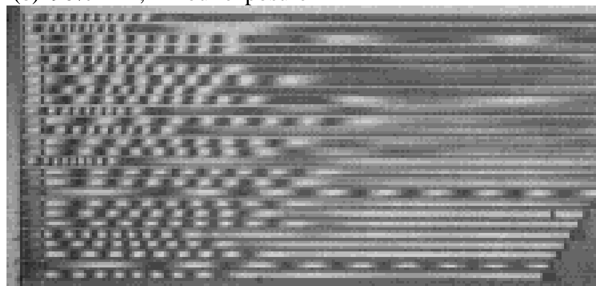
(c) 90% RH , 7 hour exposure

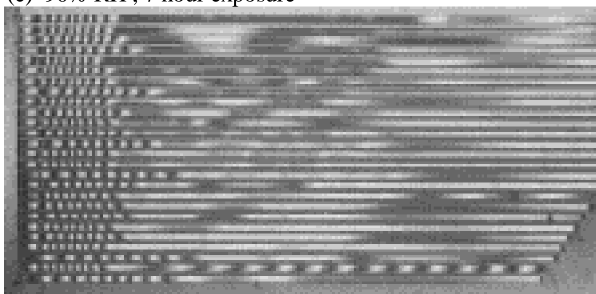
(d) 95% RH , 40 hour exposure

Fig. 11 FDTS adhesion degradation after high RH exposure

incomplete. However, it is clear from these studies that structural defects exist in these films and that structure is a sensitive function of the deposition process. This is represented by the "???" symbol in Fig. 8, suggesting that the film may not be perfectly ordered. The purpose in this portion of our work [43] is to examine the applicability to adhesion of the macroscopic description of these materials, and to gain insight into how microscopic properties may influence adhesion when the environment changes.

**5.2 The samples are coated and released by solution chemistry:** Samples were released and coated with ODTS and FDTS according to the solvent exchange procedure described in detail in ref. [44]. The contact angle with water on test samples was 112° and 115° respectively. Arrays of beams were initially freely supported above the substrate. An exposure test at increasing RH levels was conducted as follows. A voltage of 160V was gradually applied to the actuation pad to bring the beam into contact with the landing pad and brought into contact with $s\tilde{}$ 300 µm, as represented in Fig. 4. The voltage was subsequently relaxed to 0V, $s$ was allowed to increase until a stable point, and adhesion was measured. This actuation pad voltage cycle was carried out after increasing exposure times of 1 minute, 30 minutes, 4 hours, 7 hours, and 10 hours, and sometimes 40 hours. The exposure test was repeated at RH levels of 0, 30, 60, 80, 90, 95 and 99%.

The adhesion energy results are shown in Fig. 10. We see that ODTS exhibits higher adhesion energy than FDTS at from low RH values up to 80% RH. The reason for the lower adhesion of the FDTS coated samples is attributed to the lower surface energy of the less polar CF bonds compared to the CH bonds at the exposed tail group. The low values in the µJ/m$^2$ range can be attributed to the low surface energies of the coatings acting in concert with the roughness of the surfaces which causes the true contact area to be much smaller than the apparent contact area [44].

Up to 90% RH, no increase in adhesion was observed for ODTS-coated beams. At 95% RH, only a small increase in adhesion with humidity was noted for the ODTS-coated beams from approximately 7 µJ/m$^2$ to 10 µJ/m$^2$ as seen in Fig. 10. After a 48 hour exposure at 99% RH, the adhesion was observed to increase moderately to 18 µJ/m$^2$.

**5.3 For FDTS films, adhesion increases dramatically with RH:** In contrast, at 90% RH adhesion of FDTS-coated beams began to increase strongly with exposure time as seen in Fig. 11. Compared to Fig. 11(a) after 10 hour exposure at 80% RH, the effect is small but noticeable after 4 hours exposure time at 90% RH in Fig. 11(b) . A far more dramatic effect is observed in Fig. 11(c), where the

exposure time has now increased to 7 hours at 90% RH. The crack length range for various beams has decreased from 1200 to 1600 μm down to 300 to 700 microns. This corresponds to a large increase in adhesion according to the $1/s^4$ relationship of Eq. (2a). The standard deviation in adhesion $\sigma$=395 μJ/m$^2$ for Fig. 11(c) is larger than the average value $\bar{\Gamma}$=273 μJ/m$^2$, i.e. $\sigma/\bar{\Gamma}$=1.4, indicating a non-uniformity in the mechanism causing the adhesion increase. At 95% RH in Fig. 11(d), $\bar{\Gamma}$ continues to increase, while $\sigma/\bar{\Gamma}$ decreases to less than unity after a 30 hour exposure at this RH. From this one may infer that the mechanism for adhesion increase eventually effects a more uniform change across the entire surface. In Fig. 10, the increase in $\bar{\Gamma}$ as well as the sharp increase and subsequent decrease of $\sigma/\bar{\Gamma}$ is clearly seen.

Both the ODTS and FDTS coated films behave remarkably well – up to threshold values of 95 and 80% RH respectively there is very limited susceptibility to humidity. Even when the FDTS degrades, the maximum adhesion observed is only 1 mJ/m$^2$, much smaller than uncoated films at the same RH level seen in Fig. 6 above. This implies that well coated micromachine structures do not require special storage or packaging in most situations. The adhesion result is in agreement with the model of Angst and Simmons who conducted attenuated total reflection infrared (ATR-IR) measurements on ODTS films [37]. They concluded that at humidity levels up to 80% RH, water intercalates into the film but attaches mainly at silanol sites at the silica-silane interface. However, at very high levels of RH and long exposure times, the FDTS-coated beams in Fig. 11 clearly exhibit more dependence of adhesion on humidity than the ODTS-coated beams.

**5.4 Ellipsometry indicates both films adsorb water:** We conducted *in-situ* ellipsometry measurements of single crystal silicon samples subjected to increasing RH levels. Three types of surface were studied: (i) oxidized hydrophilic substrates (ii) ODTS-coated substrates and (iii) FDTS-coated substrates. The results showed that above 50% RH, water adsorbs significantly onto the hydrophilic substrate (multiple film layers), and a detectable but small adsorption of water by the ODTS and FDTS films. These results agree qualitatively with the study conducted by Angst and Simmons [37]. For the relatively short equilibration time of 10 minutes in our ellipsometer measurements, there is not a significant difference in water absorption between the ODTS and FDTS coatings. Longer times were not possible because of drift in the ellipsometer apparatus.

**5.5 Defects pervade both films:** The large difference in behavior between the two films is surprising, considering that both films are expected to contain structural defects. The density obtained during deposition is likely related to both the deposition dynamics as well as steric constraints between closely spaced molecules. Previous studies of ODTS deposition have measured packing densities of 4.2 to 4.8 per nm$^2$ [42,45] compared to a theoretical maximum packing density of 7.2 per nm$^2$ based on the van der Waals radius of the molecule and the assumptions of all-trans configuration and hexagonal close packing of the tail group [29]. For FDTS films, a density of 3.3 per nm$^2$ has been reported [45], compared to a theoretical maximum by this same calculation of 4.4 per nm$^2$. It appears that packing densities of 60-75% of maximum are achieved in coating processes similar to that used here.

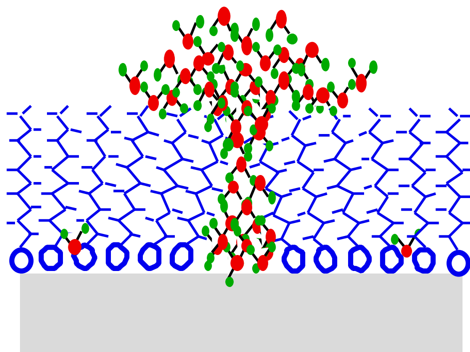

Fig. 12 Schematic of water islanding at defect site

From AFM observations on ODTS after various stages of growth, films are known to contain a variety of defects and domain structures with different density [46,47]. Low density regions with disordered tail structure (liquid expanded - LE), and domain boundaries of high density ordered regions (liquid condensed - LC), are two types of defects which must be present. Steric factors may play a role in the film density, and the degree of ordering on the tail groups. Wirth [31] and Stevens [36] have argued that close packing of tail groups in films formed from ODTS cannot be accommodated over large areas due to steric constraints. The Si-O-Si bond distance of 0.32 is smaller than the van der Waals diameter of the hydrocarbon chain, 0.4 nm, thus close packing of the tail groups would lead to unacceptable strain in the polymerized head groups. This implies that disordered regions of less than theoretical density are likely to form.

From these various observations it is clear that the observation of a large contact angle, 110° to 120°, does not necessarily indicate a densely packed array of tail groups or the complete passivation of the surface toward water adsorption. The presence of a large area fraction of disordered film and defect sites provides many opportunities for water penetration into the film, and for nucleation of water droplets at locally hydrophilic sites in the film. This local, defect controlled adsorption of water may be the source of the observed increase in adhesion energy at high RH, and the small uptake of water observed at high RH by

ellipsometry. The very small apparent film thickness observed by ellipsometry could be due to formation of many small water droplets nucleating at defect sites on the surface.

With these many possibilities for structural defects and the water uptake by both the ODTS and FDTS films, we might expect that neither film would fare well at high RH values. Yet, the ODTS film performs remarkably well. This can be attributed to the two following considerations. First, because the 18 carbon ODTS chain is longer than the 10 carbon FDTS chain, interchain bonding forces are greater, suggesting that the driving force for molecular alignment is larger for ODTS. Second, because the ODTS hydrocarbon chain is of smaller diameter than the FDTS fluorocarbon chain, one would expect that the strain induced by head group polymerization is larger in the FDTS case, also inducing a greater degree of structural imperfections. Although water intercalates into both films, defects in the FDTS films are more open, allowing greater water penetration. This allows water islands to emerge on the surface of the film, as seen in Fig. 12. If such islands from the top and bottom surfaces coalesce when the beams are brought into contact, a relatively strong adhesive bond may be formed.

**5.6 AFM reveals mounds on exposed samples:** In view of the discussion in section 5.5, we decided to compare samples that had been exposed to high RH to those which had been stored in air (in RH =50%) by atomic force microscopy (AFM) in the landing pad area. Figs. 13(a) and (b) reveal a higher density of "nanomounds" in FDTS on samples which were exposed to high RH compared to samples which were not exposed. ODTS samples exposed to high RH showed a similar result, but the density of mounds was about 10 times lower.

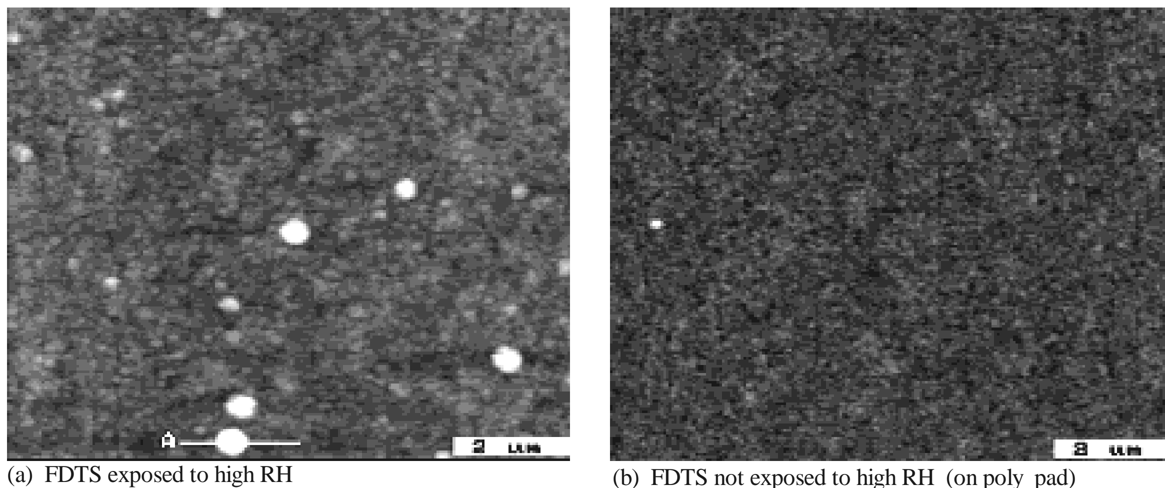


(a) FDTS exposed to high RH

(b) FDTS not exposed to high RH (on poly pad)

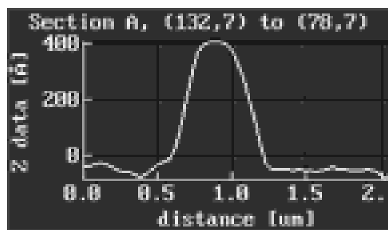


(c) linescan across large mound in (a)

Fig. 13 AFMs of FDTS films

The presence of mounds implies that high RH conditions induce further defect formation in the films, and could be responsible for the adhesion increase. Their relatively large height, 30-60 nm determined from AFM linescans as in Fig. 13(c), is unexpected in light of the above discussion, which would suggest that the defect areas would be much smaller than those we observe in Fig. 12. Beams exposed to high RH (but not actuated) exhibited low adhesion when actuated at low RH, suggesting that merely the presence of mounds does not increase adhesion. We speculate that incomplete polymerization of the head groups, perhaps in LE film regions and in the presence of high RH, allows diffusional transport of molecules across the surface to areas where three dimensional polymerization occurs to form the mounds either by lamellar or micelle formation. The mounds themselves could remain highly hydrophobic, but areas from which the molecules have migrated are then even more highly susceptible to islanding of water, as suggested in Fig. 12.

**5.7 Implications of the coatings study:** This work adds further insight to the question of which molecule, ODTS or FDTS, is more appropriate in packaged MEMS applications. Other work [44] suggests that FDTS might be favored because it is less susceptible to oxidation at temperatures up to 400 °C. However, even hermetically sealed packages may eventually allow penetration of water, and this possibility should be considered when assessing the long term reliability of MEMS devices.

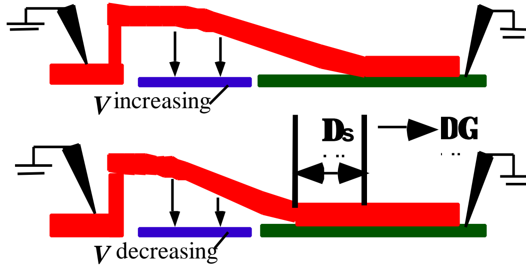


Fig. 14 Adhesion hysteresis concept

## 6. DEVELOPMENT OF NEW MECHANICS TO MEASURE ADHESION HYSTERESIS

**6.1 Actuation was required to observe adhesion increase.** For the uncoated beams, we saw in section 4 that capillary forces at the crack tip caused cracks to heal noticeably with time, and equilibrium was reached in approximately 40 hours. Such spontaneous crack healing was not observed on the coated beams in section 5. Rather, actuation was required for the adhesion increase to exhibit itself. However, from mechanics considerations, the crack should heal if the adhesion increase is uniform along the length of the beam.

**6.2 How to measure adhesion hysteresis.** How are the surface forces which bring about the adhesion hysteresis behavior activated? Answering this question would improve our understanding of the breakdown mechanism of the molecular coating at high RH, and perhaps explain the origin of the hysteresis. By measuring the adhesion in the presence of the external force, we can quantifiably determine just when this occurs, and quantify the magnitude of the adhesion hysteresis during crack healing (increasing pad voltage) and crack propagation (decreasing pad voltage). The idea is presented in Fig. 14. At a given voltage level, the length *s* can be calculated from beam mechanics in the absence of adhesion. If adhesion exists, then *s* will be smaller, and the beam deflections will be significantly different. Because we measure global deflections of the beam with interferometry, adhesion can be extracted to high confidence by matching the experimental data to finite element simulations of beam deflections at different adhesion values. Details of the technique will be provided in ref. [48].

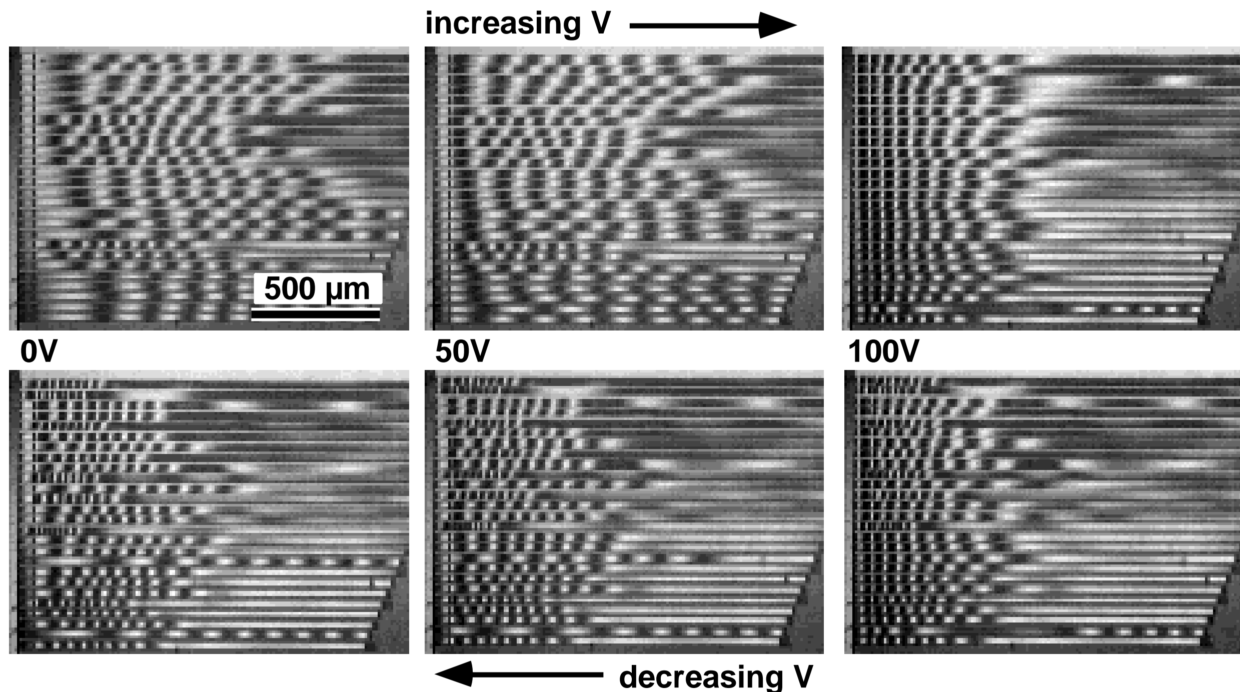


Fig. 15 Interferograms taken at 0, 50 and 100V on the actuation pad for increasing and decreasing voltage. Actuation cycle is after 7 hours exposure to 90% RH.

Interferograms in the experiment of section 5 were also recorded at intermediate voltages of the actuation pad at levels of 50, 100, 120, 140 and 160V in addition to the images taken at 0V. The data during the large change in adhesion of FDTS after 7 hours (Fig. 11(b) to (c)) is shown in Fig. 15 above. At decreasing voltages of 100, 50 and 0V, the propagating crack lengths are much shorter than the healing crack lengths at increasing voltages. For example, at 50V during the voltage increase, crack lengths are 800-1300 µm long, while at 50V during the voltage decrease, the crack lengths are only 300-500 µm long.

At each voltage, the simulated curve shapes are compared to the experiment using a least squares fit, and the best value for adhesion is chosen. Typical model fits of beam deflections including both external force applied by the actuation pad as well as adhesion are shown for one beam in Fig. 16.

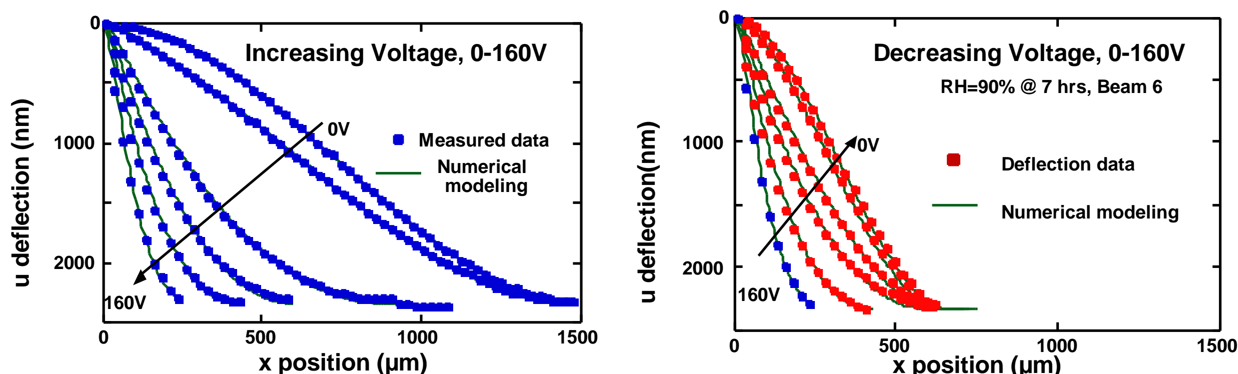


Fig. 16 Finite element model fits to the data for one beam. The actuation pad voltage is set to the measured value, and the adhesion is varied until the least square error with the deflection curve is minimized.

**6.3 Hysteresis results interpreted in terms of adhesion non-uniformity.** In Fig. 17, we show adhesion versus voltage for four representative individual beams during this activation cycle (the beam numbers are counted from the top of Fig. 15). As seen in Fig. 11, not all beams exhibit the same adhesion behavior. Hence it is quite reasonable to observe that adhesion varies along the length of the beam as well.

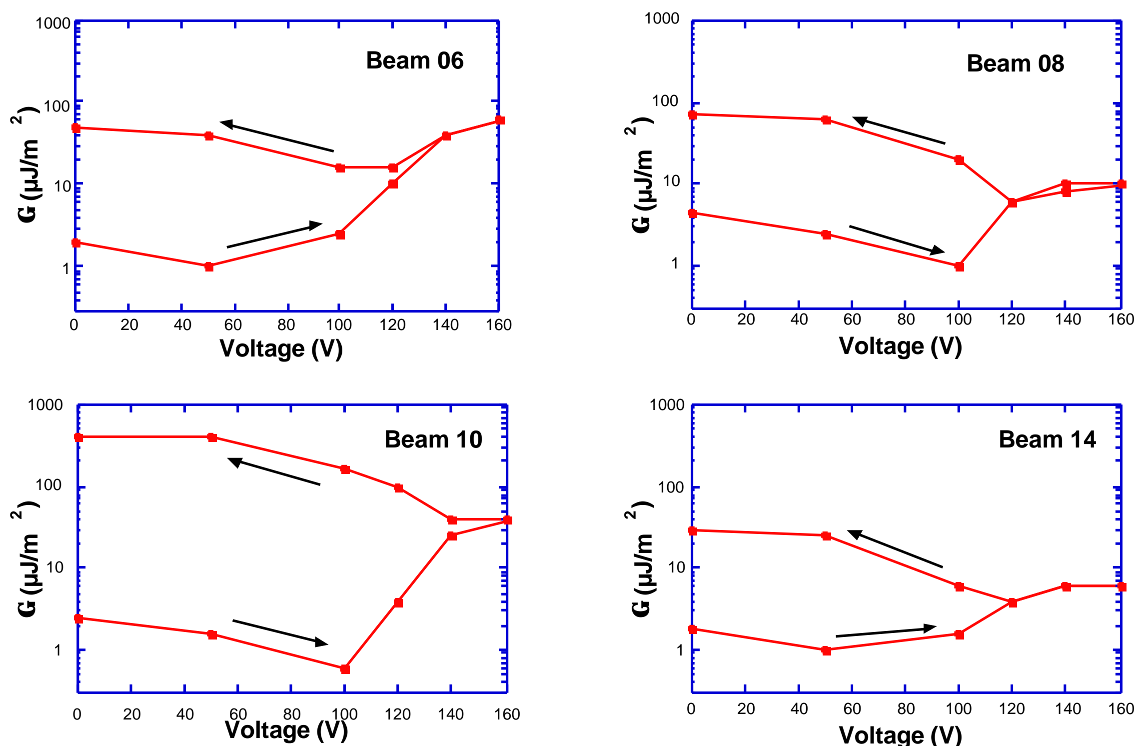


Fig. 17 Adhesion hysteresis curves for four different beams are interpreted below.

The adhesion hysteresis curves can be interpreted in terms of the defect mechanism:

A) Crack healing (increasing voltage)

i) As voltage is increased from 0 to 50V, Γ decreases from ~3 to ~1 μJ/m$^2$, while the crack length remains the same. The increase from 0 to 50V provides only a small crack healing force. If adhesion were constant at 3 μJ/m$^2$, the crack would heal approximately 200 μm. This indicates that in the vicinity of the crack tip, surface forces are not locally available to do work on the beam. We can understand this in the following

sense: if there are small differences in local adhesion along the length of the beam (e.g., due local differences in roughness or FDTS surface coverage), the crack will have propagated until it found a locally higher value of adhesion during its previous cycle.

ii) When pad voltage is increased to 100 V, the crack is forced to heal, and $\Gamma$ sometimes increases and sometimes decreases relative to the values at 0 and 50V. If the crack reaches an area of locally high adhesion, surface forces will do more work on the beam to pull it further in, resulting in a larger value of adhesion. If the local adhesion is small, a lower value of adhesion results.

iii) In most cases, $\Gamma$ increases monotonically as applied voltage is increased beyond 100V up to 160V. This indicates a local increase in the adhesion. This could be due to a local increase the adhesion in this area. However, a more interesting mechanism may be have taken place. Namely, at the higher voltages, more compression at the crack tip is initially exerted before surface forces subsequently pull the beam in to attain equilibrium. The compression may cause spreading of water islands over the surface or an increase in contact area of the polymer globules, which would act to increase the adhesion.

B) Crack propagation (decreasing voltage)

i) As voltage is lowered down to 140 and sometimes to 100V, adhesion $\Gamma$ may increase or decrease, but is equal to or greater than the value of $\Gamma$ for the increasing voltage. Because the applied voltages are discrete, defect sites which enhance the adhesion are not necessarily activated upon crack healing. However, upon crack propagation, they have been activated - hence the resulting hysteresis.

ii) Below a value of voltage between 140 and 100V, the adhesion $\Gamma$ increases monotonically. This is because as the voltage is lowered, the crack tip eventually encounters a region where the local adhesion is high enough that the remaining restoring force in the beam is too small to further extend the crack, and the crack length remains unchanged.

## 7. SUMMARY AND FUTURE WORK

Adhesion in MEMS is a critical parameter for system reliability. To quantify reliability, it is important to understand the limitations of applied coatings with respect to ambient. In this paper, we have reported on a fundamental approach to study adhesion using interferometry *in-situ* on actuated cantilever beams. The main lessons we have learned are:

1) In-situ interferometry of activated devices is a critical tool in assessing adhesion in MEMS. It allows direct confirmation of beam deflections, allowing accurate assessment of adhesion energies.
2) The S-shape cantilever beam is preferred over the arc-shape beam for fundamental adhesion studies.
3) For uniformly hydrophilic surfaces, adhesion is exponentially dependent upon humidity. This is due to surface roughness. A single asperity model serves well to describe this trend. The adhesion values for hydrophilic surfaces are far too high for MEMS applications. Therefore, a hydrophobic coating is required.
4) For hydrophobic surfaces created by the application of silane coupling agents, adhesion remains independent of humidity up to a threshold level of 80-95% depending on the coating.
5) A defect mechanism appears to be responsible for the adhesion increase above this threshold level. Local areas of the film may be susceptible to islanding of water. Polymeric globules appear on samples exposed to high RH, which may increase the susceptibility to water islanding.
6) We developed mechanics for measurement of adhesion in the presence of an external force, enabling us to quantify adhesion hysteresis. Our adhesion hysteresis measurements can be interpreted in terms of non-uniform adhesion along the length of the beam, in agreement with the defect mechanism for adhesion increase.

While we have made progress in understanding adhesion in MEMS, many issues deserve further research. Some of these are: (1) How do various types of roughness affect the exponential trend with humidity for hydrophilic surfaces? (2) The work reported here was for static adhesion. By measuring adhesion dynamics, can we predict the performance of delaminating components in MEMS applications? (3) Can we relate the adhesion hysteresis measurements to frictional properties, as is done with the surface forces apparatus [49,50]? (4) Nitride films are often used in MEMS, but susceptible to charging. Can we model this charging using interferometric data to learn more about its nature? (5) Can we develop hydrophobic coatings which are less susceptible to water adsorption and wear?

## 8. ACKNOWLEDGEMENTS

Sandia is a multiprogram laboratory operated by Sandia Corporation, a Lockheed Martin Company, for the United States Department of Energy under Contract DE-AC04-94AL85000. We thank Uthara Srinivasan and Roya Maboudian of UC Berkeley for providing the ODTS and FDTS-coated samples, Robert Carpick at SNL for taking

the AFM images, and Bruce Bunker at SNL for discussions on monolayer defects. We also thank the staff at the Microelectronics Development Laboratory at Sandia National Laboratories for fabricating and releasing the other samples in this work.

## 9. REFERENCES

[1] T. A. Roessig, R. T. Howe, A. P. Pisano and J. H. Smith, "*Surface-Micromachined Resonant Accelerometer*," presented at Transducers '97, Chicago, IL, USA, 1997, pp. 859-862.

[2] T. Juneau, A. P. Pisano and J. H. Smith, "*Dual axis operation of a micromachined rate gyroscope*," presented at Transducers '97, Chicago, IL, USA, 1997, pp. 883-886.

[3] A. Lawrence, *Modern Inertial Technology* (Springer Verlag, New York, 1993).

[4] L. J. Hornbeck, "*Projection displays and MEMS: timely convergence for a bright future*," presented at SPIE '95, Austin, TX, 1995, pp. 2.

[5] J. J. Sniegowski, "*Multi-level polysilicon surface-micromachining technology: applications and issues*," presented at ASME IMECE, Atlanta, GA, Nov. 1996, 1996, pp. 751-759.

[6] J. J. Allen and H. K. Schriner, "*Micromachine Wedge Stepping Motor*," presented at ASME IMECE, Anaheim, CA, 1998, pp. 317-321.

[7] M. S. Rodgers, (see www.mdl.sandia.gov/Micromachine, 1999).

[8] J. J. Sniegowski and E. J. Garcia, "*Microfabricated Actuators and Their Application to Optics*," presented at Miniaturized Systems with Micro-Optics and Micromechanics, San Jose, CA, 1995, pp. 46-64.

[9] S. Y. Lin *et al.*, "*A 3-dimensional photonic crystal operating at infrared wavelengths*," Nature **394** (6690), 251 (1998).

[10] J. G. Fleming and S. Y. Lin, "*Three-dimensional photonic crystal with a stop band from 1.35 to 1.95 μm*," Opt. Lett. **24** (1), 49 (1999).

[11] M. S. Rodgers and J. J. Sniegowski, "*Five-level polysilicon surface micromachine technology: application to complex mechanical systems*," presented at Hilton Head '98, Hilton Head Island, SC, USA, 1998, pp. 144-149.

[12] J. H. Smith, S. Montague, J. J. Sniegowski, J. R. Murray and P. J. McWhorter, "*Embedded Micromechanical Devices for the Monolithic Integration of MEMS with CMOS*," presented at IEDM, Washington, 1995, pp. 609-612.

[13] B. D. Jensen, M. P. de Boer and S. L. Miller, "*IMaP: Interferometry for materials property evaluation in MEMS*," presented at MSM '99, San Juan, Puerto Rico, 1999, pp. 206-209.

[14] M. P. de Boer and T. A. Michalske, "*Accurate method for determining adhesion of cantilever beams*," J. Appl. Phys. **86** (2), 15 July (1999).

[15] C. H. Mastrangelo and C. H. Hsu, "*A simple experimental technique for the measurement of the work of adhesion of microstructures*," presented at Hilton Head, 1992, pp. 208-214.

[16] R. L. Alley, P. Mai, K. Komvopoulos and R. T. Howe, "*Surface roughness modification of interfacial contacts in polysilicon microstructures*," presented at Transducers '93, 1993, pp. 288-291.

[17] R. Legtenberg, J. Elders and M. Elwenspoek, "*Stiction of surface micromachining structures after rinsing and drying: model and investigation of adhesion mechanisms*," presented at Transducers '93, 1993, pp. 298-301.

[18] M. R. Houston, R. T. Howe and R. Maboudian, "*Effect of hydrogen termination on the work of adhesion between rough polycrystalline silicon surfaces*," J. Appl. Phys. **81** (8), 3474 (1997).

[19] Y. Yee, K. Chun and J. D. Lee, "*Polysilicon surface modification technique to reduce sticking of microstructures*," presented at Transducers '95, 1995, pp. 206-209.

[20] Y. Yee, M. Park and K. Chun, "*A sticking model of suspended polysilicon microstructure including residual stress gradient and postrelease temperature*," J. MEMS **7** (3), 339 (1998).

[21] U. Srinivasan *et al.*, "*Lubrication of polysilicon micromechanisms with self-assembled monolayers*," presented at Hilton Head '98, Hilton Head Island, SC, USA, 1998, pp. 156-161.

[22] K. L. Johnson, K. Kendall and A. D. Roberts, "*Surface energy and the contact of elastic solids*," Proc. Roy. Soc. Lond. A. **324**, 301 (1971).

[23] W. N. Sharpe, R. Vaidyanathan, B. Yuan, G. Bao and R. L. Edwards, "*Effect of etch holes on the mechanical-properties of polysilicon*," J. Vac. Sci. Tech. **15** (5), 1599 (1997).

[24] Q. Meng, M. Mehregany and R. L. Mullen, "*Theoretical modeling of microfabricated beams with elastically restrained supports*," J. MEMS **2** (3), 128 (1993).

[25] B. C. Bunker and T. A. Michalske, "*Effect of surface corrosion on glass fracture*," in *Fracture Mechanics of Ceramics*, edited by R. C. Bradt, A. G. Evans, D. P. H. Hasselman *et al.* (Plenum Press, New York, 1986), Vol. 8, pp. 391-411.

[26] G. T. Mulhern, D. S. Soane and R. T. Howe, "*Supercritical carbon dioxide drying of microstructures*," presented at Transducers '93, 1993, pp. 296-299.

[27] M. P. de Boer, P. J. Clews, B. K. Smith and T. A. Michalske, "*Adhesion of polysilicon microbeams in controlled humidity ambients*," Mater. Res. Soc. Proc. **518**, 131 (1998).

[28] T. A. Michalske and E. R. Fuller, "*Closure and repropagation of healed cracks in silicate glass*," J. Am. Ceram. Soc. **68** (11), 586 (1985).

[29] J. Israelachvili, *Intermolecular and Surface Forces* (Academic Press, New York, 1992).

[30] N. G. Cave and A. J. Kinloch, "*Self-assembling monolayer silane films as adhesion promoters*," Polymer **33** (6), 1162 (1992).

[31] M. J. Wirth, R. W. P. Fairbank and H. O. Fatunmbi, "*Mixed self-assembled monolayers in chemical separations*," Science **275**, 44 (1997).

[32] V. DePalma and N. Tillman, "*Friction and wear of self-assembled tricholorosilane monolayer films on silicon*," Langmuir **5**, 868 (1989).

[33] J. Ruehe, V. J. Novotny, K. K. Kanazawa, T. Clarke and G. B. Street, "*Structure and tribological properties of ultrathin alkylsilane films chemisorbed to solid surfaces*," Langmuir **9**, 2383 (1993).

[34] M. R. Houston, R. Maboudian and R. T. Howe, "*Self-assembled monolayer films as durable anti-stiction coatings for polysilicon microstructures*," presented at Hilton Head '96, Hilton Head Island, SC, USA, 1996, pp. 42-47.

[35] M. Mehregany, S. D. Senturia and J. H. Lang, "*Measurement of wear in polysilicon micromotors*," IEEE Trans. Electron Devices **39** (5), 1136 (1992).

[36] M. J. Stevens, "*Thoughts on the structure of alkylsilane monolayers*," Langmuir **15**, 2773 (1999).

[37] D. L. Angst and G.W. Simmons, "*Moisture absorption charateristics of organosiloxane self-assembled monolayers*," Langmuir **7**, 2236 (1991).

[38] A. N. Parikh, D. L. Allara, I. B. Azouz and F. Rondelez, "*An intrinsic relationship between molecular structure in self-assembled n-alkylsiloxane monolayers and deposition temperature*," J. Phys. Chem. **98**, 7577 (1994).

[39] M. E. McGovern, K. M. R. Kallury and M. Thompson, "*Role of solvent on the silanization of glass with octadecyltrichlorosilane*," Langmuir **10**, 3607 (1994).

[40] C. P. Tripp and M. L. Hair, "*Reaction of alkylchlorosilanes with silica at the solid/gas and solid/liquid interface*," Langmuir **8**, 1961 (1992).

[41] C. P. Tripp and M. L. Hair, "*Direct observation of the surface bonds between self-assembled monolayers of octadecyltrichlorosilane and silica surfaces: a low frequency IR study at the solid/liquid interface*," Langmuir **11**, 1215 (1995).

[42] S. R. Wasserman, G. M. Whitesides, I. M. Tidswell, B. M. Ocko, P. S. Pershan and J. D. Axe, "*The structure of self-assembled monolayers of alkylsiloxanes on silicon: a comparison of results from ellipsometry and low-angle x-ray reflectivity*," J. Am. Chem. Soc. **111**, 5852 (1989).

[43] M. P. de Boer, T. M. Mayer, T. A. Michalske, U. Srinivasan and R. Maboudian, "*Adhesion performance of silane coupling agents at high humidity levels*," Acta Mater. **submitted** (1999).

[44] U. Srinivasan, M. R. Houston, R. T. Howe and R. Maboudian, "*Alkyltrichlorosilane-based self-assembled monolayer films for stiction reduction in silicon micromachines*," J. Micromech. Sys. **7** (2), 252 (1998).

[45] R. Banga, J. Yarwood, A. M. Morgan, B. Evans and J. Kells, "*In-situ FTIR studies of the kinetics and self-assembly of alkyl and perfluro alkyl trichlorosilanes on silicon*," Thin Solid Films **284-285**, 261 (1996).

[46] C. Carraro, O. W. Yauw, M. M. Sung and R. Maboudian, "*Observation of three growth mechanisms in self-assembled monolayers*," J. Phys. Chem. B **102** (23), 4441 (1998).

[47] J. B. Brzoska, I. B. Azouz and F. Rondelez, "*Silanization of solid substrates: a step towards reproducibility*," Langmuir **10**, 4376 (1994).

[48] M. P. de Boer, J. A. Knapp, T. A. Michalske, U. Srinivasan and R. Maboudian, "*Adhesion hysteresis of coated polysilicon beams in controlled humidity ambients*," to be submitted (1999).

[49] Y. L. Chen, M. L. Gee, C. A. Helm, J. N. Israelachvili and P. M. McGuiggan, "*Effects of humidity on the structure and adhesion of amphiphilic monolayers on mica*," J. Phys. Chem. **93**, 7057 (1989).

[50] Y. L. Chen and J. N. Israelachvili, "*Effects of ambient conditions on adsorbed surfactant and polymer monolayers*," J. Phys. Chem. **96**, 7752 (1992).